Nanoscale

ROYAL SOCIETY
OF CHEMISTRY

PAPER
Min Jae Ko, Yung-Eun Sung *et al.*
Highly uniform and vertically aligned SnO₂ nanochannel arrays for
photovoltaic applications

NCNST

Highly uniform and vertically aligned SnO₂ nanochannel arrays for photovoltaic applications†

Jae-Yup Kim,‡[a] Jin Soo Kang,‡[b,c] Junyoung Shin,[c] Jin Kim,[b,c] Seung-Joo Han,[d] Jongwoo Park,[a] Yo-Sep Min,[d] Min Jae Ko*[a,e,f] and Yung-Eun Sung*[b,c]

Nanostructured electrodes with vertical alignment have been considered ideal structures for electron transport and interfacial contact with redox electrolytes in photovoltaic devices. Here, we report large-scale vertically aligned SnO₂ nanochannel arrays with uniform structures, without lateral cracks fabricated by a modified anodic oxidation process. In the modified process, ultrasonication is utilized to avoid formation of partial compact layers and lateral cracks in the SnO₂ nanochannel arrays. Building on this breakthrough, we first demonstrate the photovoltaic application of these vertically aligned SnO₂ nanochannel arrays. These vertically aligned arrays were directly and successfully applied in quasi-solid state dye-sensitized solar cells (DSSCs) as photoanodes, yielding reasonable conversion efficiency under back-side illumination. In addition, a significantly short process time (330 s) for achieving the optimal thickness (7.0 μm) and direct utilization of the anodized electrodes enable a simple, rapid and low-cost fabrication process. Furthermore, a TiO₂ shell layer was coated on the SnO₂ nanochannel arrays by the atomic layer deposition (ALD) process for enhancement of dye-loading and prolonging the electron lifetime in the DSSC. Owing to the presence of the ALD TiO₂ layer, the short-circuit photocurrent density (J_{sc}) and conversion efficiency were increased by 20% and 19%, respectively, compared to those of the DSSC without the ALD TiO₂ layer. This study provides valuable insight into the development of efficient SnO₂-based photoanodes for photovoltaic application by a simple and rapid fabrication process.

Introduction

Nanostructured transition metal oxides prepared by electrochemical anodic oxidation have received significant attention for diverse applications in nanomaterial synthesis,[1–3] photonic crystals,[4,5] biosensors,[6,7] and photovoltaics,[8–20] owing to their unique properties stemming from their one-dimensional geometry and vertically aligned pore structures, as well as the advantages of the anodic oxidation process such as simplicity,

[a]*Photo-electronic Hybrids Research Center, Korea Institute of Science and Technology (KIST), Seoul 136-791, Republic of Korea. E-mail: mjko@kist.re.kr; Fax: +82-2-958-6649; Tel: +82-2-958-5518*

[b]*Center for Nanoparticle Research, Institute for Basic Science (IBS), Seoul 151-742, Republic of Korea. E-mail: ysung@snu.ac.kr; Fax: +82-2-888-1604; Tel: +82-2-880-1889*

[c]*School of Chemical and Biological Engineering, Seoul National University, Seoul 151-742, Republic of Korea*

[d]*Department of Chemical Engineering, Konkuk University, Seoul, 143-701, Republic of Korea*

[e]*Green School, Korea University, Seoul 136-701, Republic of Korea*

[f]*KU-KIST Graduate School of Converging Science and Technology, Korea University, Seoul 136-701, Republic of Korea*

†Electronic supplementary information (ESI) available. See DOI: 10.1039/c5nr00202h

‡These authors contributed equally to this work.

reliability, and low cost for large-scale production. Firstly, anodic aluminum oxides (AAOs) prepared by anodic oxidation of Al have been studied over the last six decades, especially in the field of nanotechnology. In addition, since Macák *et al.* first used highly ordered TiO₂ nanotube arrays, prepared by anodic oxidation of Ti as photoanodes in dye-sensitized solar cells (DSSCs),[8] the optimization and application of these TiO₂ nanotube or nanochannel arrays for photovoltaic devices have been intensively studied.[9–17] Vertically oriented nanotube or nanochannel electrodes have been considered as ideal structures for electron transport in photovoltaic devices; indeed, it was shown that these one-dimensional structures exhibit a lower electron recombination rate and a stronger light scattering effect than the conventional randomly oriented structures based on spherical nanoparticles.[10] Furthermore, vertically aligned pore structures are advantageous for the diffusion of redox couples and interfacial contacts with electrolytes or hole conductors in photovoltaic devices.[12,14]

Although, besides Al and Ti, anodic oxidation of other transition metals such as Nb,[18,21] Zr,[22,23] W,[24,25] Ta,[26] Hf,[27] and Sn[28–31] for the formation of vertically aligned nanotube or nanochannel metal oxide arrays has been reported, the studies and applications have been relatively insufficient for these metals compared to the cases of Al and Ti. In particular, verti-

cally aligned SnO$_2$ nanochannel arrays might be an attractive material for photovoltaic applications. Although the electron recombination rate in SnO$_2$ is faster by two to three orders of magnitude[32] and the conversion efficiency is poorer than those of the conventional TiO$_2$ as a photoanode material in mesoscopic sensitized solar cells (dye- or quantum dot-sensitized solar cells), it has received much attention due to its potential properties such as faster electron transport rate and tolerance to UV illumination resulting from the larger band gap (3.6 eV, cf. TiO$_2$ ∼3.2 eV).[32–39] In addition, because the conduction band potential of SnO$_2$ is 0.4 eV more positive than that of TiO$_2$, electron injection becomes possible from dyes or inorganic sensitizers (quantum dots) that are energetically unfavorable with respect to TiO$_2$.[36–38]

However, a direct application of anodic SnO$_2$ nanochannel arrays maintaining vertically aligned structures as photoelectrodes in photovoltaic devices has not been reported yet. This is due to the difficulty of fabricating anodic SnO$_2$ electrodes with uniform nanoporous structures over large areas without lateral cracks. Because the Sn anodic oxidation process is very fast in general,[28] it is difficult to fabricate anodic SnO$_2$ electrodes with nanoporous surface structures over large areas. In addition, due to the vigorous oxygen evolution during the Sn anodic oxidation process, many lateral cracks are generated, resulting in a discontinuous nanochannel structure composed of stacked layers several hundreds of nanometers thick.[28–31] Although Hossain et al.[40] and Teh et al.[41] reported mesoscopic sensitized solar cells employing anodic nanoporous SnO$_2$ as photoanode materials, they could not directly utilize anodic nanoporous SnO$_2$ maintaining vertically aligned structures. Instead, these researchers peeled off the anodic nanoporous SnO$_2$ from the Sn metal substrate, and then used the peeled material to prepare a paste for deposition onto the conductive substrate (FTO glass), resulting in a randomly oriented structure of the photoanode material.

In this study, we developed a modified process of Sn metal anodic oxidation for fabrication of large-scale SnO$_2$ nanochannel arrays with uniform structures but without lateral cracks. The Sn anodic oxidation process was performed in an oxalic acid solution with the assistance of ultrasonication. Using ultrasonication, a uniform nanoporous structure was formed over large surface areas and lateral cracks were not generated, yielding vertically aligned continuous nanochannel arrays. These nanochannel arrays were directly used in quasi-solid state DSSCs as photoanodes. To the best of our knowledge, it is the first photovoltaic application of vertically aligned anodic SnO$_2$ nanochannel arrays. The thickness of SnO$_2$ nanochannel arrays was controlled by varying the anodic oxidation time. Photovoltaic performances were examined for SnO$_2$ nanochannel arrays with different thicknesses. Owing to the significantly short anodic oxidation time (330 s) for achieving the optimal thickness (7.0 μm) for photovoltaic performance, and owing to the utilization of a gel-type electrolyte, the devices in this study were fabricated through a simple and rapid process. Furthermore, in order to enhance the photovoltaic performance, a TiO$_2$ shell layer was deposited onto the SnO$_2$ nanochannel by atomic layer deposition (ALD). The enhanced photovoltaic properties, in particular the prolonged electron lifetime resulting from the TiO$_2$ shell addition, were characterized.

Experimental

Preparation of SnO$_2$ and SnO$_2$/TiO$_2$ nanochannel arrays

Vertically aligned SnO$_2$ nanochannel arrays were fabricated by using a modified anodic oxidation method. Tin foil (Alfa Aesar, 99.8% purity, 0.25 mm thick, 2.0 cm × 1.5 cm in size) was anodized in a 0.5 M oxalic acid aqueous solution.[28] The anodic oxidation process was carried out under ultrasonication (60 W, 28 kHz, MUJIGAE SD-120H). Pt mesh was used as a counter electrode, and the distance between the tin foil and Pt mesh was 5 cm. A dc potential of 10 V was applied and the anodic oxidation time was varied from 90 to 390 s. The as-anodized SnO$_2$ electrode was washed in distilled water under ultrasonication, followed by thermal annealing at 500 °C for 3 h in air. The TiO$_2$ shell layer was grown on the surface of SnO$_2$ nanochannel arrays at 150 °C by using a laminar flow type ALD reactor. One ALD cycle for TiO$_2$ consists of four steps: TiCl$_4$ exposure (1 s) – purging (5 s) – H$_2$O exposure (1 s) – purging (20 s). The ALD cycle was repeated for growing the ultrathin TiO$_2$ with thicknesses of 1, 2, 5, and 10 Å. For each TiO$_2$ thickness, the ALD process was repeated for 3, 6, 15, and 30 cycles considering the growth-per-cycle of 0.34 Å per cycle measured on bare Si wafers. TiCl$_4$ (UP Chemical Co., Ltd) and H$_2$O were vaporized from external canisters at room temperature and led into the reactor through solenoid valves without any carrier gas. High-purity N$_2$ gas (99.999%) was used as a purging gas with a flow rate of 400 sccm. All delivery lines were maintained at 120 °C. The base pressure of the reactor was below 10 mTorr and ALD was performed at a working pressure of 200–600 mTorr.

Characterization of materials

The morphology and the structure of the SnO$_2$ nanochannel arrays were examined using a field-emission scanning electron microscope (FE-SEM; Carl Zeiss SUPRA 55VP), and a transmission electron microscope (TEM; JEOL JEM-2010). The cross-sectional images of the SnO$_2$ nanochannel arrays were obtained using an FE-SEM (Cal Zeiss AURIGA) after focused ion beam (FIB) milling. The chemical states were confirmed from elemental energy-filtered (EF)-TEM maps (JEOL JEM-2100F). The crystalline phase was confirmed using high power X-ray diffraction (XRD; Rigaku D/MAX 2500 V diffractometer) with Cu Kα radiation. The surface compositions were characterized by using X-ray photoelectron spectroscopy (XPS; Thermo SIGMA PROBE), using an Al Kα X-ray source in an UHV system with a chamber base pressure of ∼10^{-10} Torr.

Fabrication of solar cells

The prepared SnO$_2$ nanochannel electrodes were dipped into a 5 × 10^{-4} M N-719 dye (Ru 535-bisTBA, Solaronix) solution in ethanol for 24 h at room temperature. The Pt-counter electro-

des were prepared by spin-casting a drop of 10 mM H_2PtCl_6 in 2-propanol onto F-doped SnO_2 (FTO) glass followed by heat treatment at 400 °C for 15 min in air. A thermal adhesive film (Surlyn, thickness: 30 μm) was attached on the dye-adsorbed SnO_2 electrodes. A commercial gel-type electrolyte containing I^-/I_3^- redox couples (EL-SGE, Dyesol) was cast on the dye-adsorbed SnO_2 electrodes, followed by covering with Pt-counter electrodes with the aid of clamps.
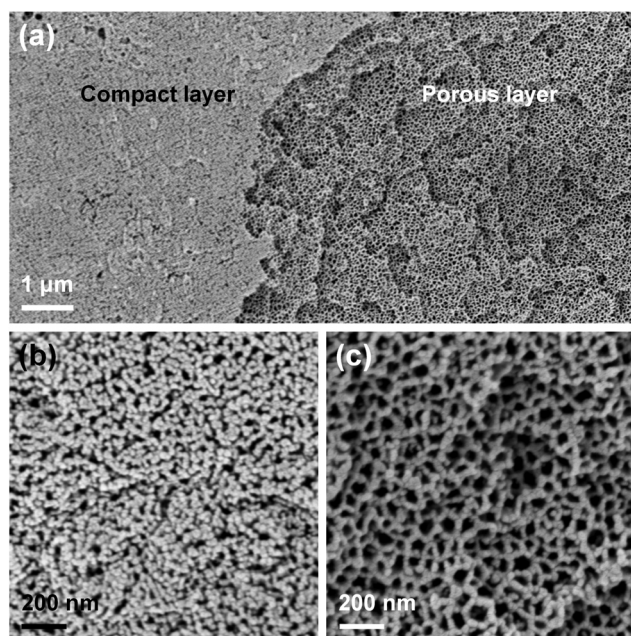
Characterization of solar cells

Standard photocurrent density–voltage (J–V) measurements were performed using a 500 W xenon lamp (XIL model 05A50KS source measure units and an AM 1.5G filter) at a power of 100 mW cm^{-2} and a potentiostat (Solartron 1480). The solar cells were covered with a black aperture mask before the measurements in order to avoid the additional illumination through the lateral space.[42,43] The electrochemical impedance spectra were obtained in the dark with the bias potential of −0.5 V using a Zahner IM6. The magnitude of the sinusoidal perturbations was 10 mV, and the frequency ranged from 0.1 Hz to 100 kHz.
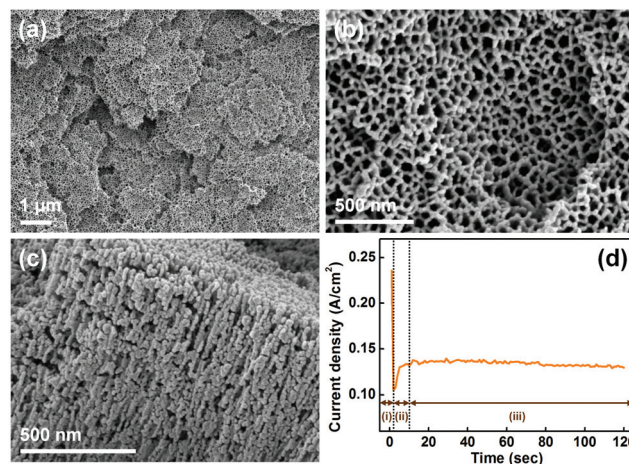
Results and discussion

Fig. 1 shows field emission-scanning electron microscopy (FE-SEM) images of annealed SnO_2 nanochannel arrays prepared by the conventional anodic oxidation process (at 10 V for 330 s, without ultrasonication) according to a previous report.[28] As shown in Fig. 1a, the Sn substrate surface was not uniformly anodized over large areas. Porous layers and relatively compact layers coexisted, and we found this trend to be consistent throughout the whole areas of the samples. A nanochannel structure with a pore size of 50–80 nm and a wall thickness of 20–30 nm was observed in the porous layers. However, the coexisting compact layers did not seem to be sufficiently porous to be utilized as photoanodes of mesoscopic sensitized solar cells.

On the other hand, the samples prepared by anodic oxidation with ultrasonication (at 10 V for 330 s) had uniform nanochannel structures over large areas, as shown in Fig. 2a. Compact layers were not observed throughout the whole areas of these samples. As shown in Fig. 2b, the pore size and wall thickness were identical to those of the samples prepared by using the conventional method. Fig. 1c shows the cross-sectional image of SnO_2 nanochannel arrays, representing the vertically aligned pore structure and partially one-dimensional walled structure. Fig. 2d shows the current transient during the Sn anodic oxidation, exhibiting a profile similar to that of other valve metals. However, compared to the well-known anodic oxidation processes (such as anodic oxidation of Ti and Al), the time-scale was significantly short, implying the rapid reaction process. For example, the step for the initial formation of compact oxide layers (step (i) in Fig. 2d) generally takes about 5–10 minutes in the anodic oxidation process of Ti;[44] however, in this work, the same step for Sn took only about only 2 s. This rapid anodic oxidation process accompanied by vigorous oxygen evolution[28] led to nonhomogeneous distribution of chemical and field-assisted dissolution throughout the surface, resulting in the formation of a non-

Fig. 1 FE-SEM images of annealed SnO_2 nanochannel arrays prepared by using the conventional anodic oxidation process. (a) Low-magnification surface image. (b) High-magnification image of a compact layer in (a). (c) High-magnification image of a porous layer in (a).

Fig. 2 (a) Low-magnification surface FE-SEM image of annealed SnO_2 nanochannel arrays prepared by ultrasonication. (b) High-magnification image of (a). (c) Cross-sectional image of annealed SnO_2 nanochannel arrays prepared by ultrasonication. (d) Current transient during anodic oxidation of Sn foil by ultrasonication. Step (i): formation of compact SnO_2 layers; step (ii): chemical and field-assisted dissolution of the formed oxide layer resulting in nucleation of nanopores; step (iii): formation of porous nanochannel structures.

uniform pore structure when the conventional method was applied. However, by ultrasonication, ultrasonic waves assisted the oxygen gas to escape rapidly and smoothly, leading to homogeneous distribution of chemical and field-assisted dissolution of the formed SnO_2 layers throughout the whole surface.[45] As a result, a uniform pore structure was formed by ultrasonication as shown in Fig. 2a.

Fig. 3a shows the X-ray diffraction (XRD) patterns for the prepared SnO_2 nanochannel arrays before and after annealing. The as-anodized sample exhibited nearly the same pattern as the Sn foil, indicating that the as-anodized sample has an amorphous phase. After annealing at 500 °C for 3 h in air, the sample was crystallized and it exhibited a pattern corresponding to the cassiterite SnO_2 phase.[46,47] The (101) peak corresponding to the Sn metal still remained, because the Sn foil was located beneath the SnO_2 layer. The average crystallite size calculated by using the Scherrer equation[48] was about 22.7 nm. Fig. 3b and c show the transmission electron microscopy (TEM) images of the annealed sample. The nanochannel structures were confirmed again as already observed in the FE-SEM images. Fig. 3b shows the top view of the SnO_2 nanochannel with a pore size of 50–80 nm and a wall thickness of 20–30 nm, which accorded with the FE-SEM images. Fig. 3c shows the lateral view of the SnO_2 nanochannel, exhibiting a one-dimensional walled structure. In addition, the crystal phase was cross-checked by using the selected area electron diffraction (SAED) pattern as shown in Fig. 3d, which is consistent with the XRD pattern presented in Fig. 3a.

Since the thickness of the photoanode can greatly affect the photovoltaic performance of mesoscopic sensitized solar cells,[49,50] we precisely measured the dependence of the SnO_2 nanochannel array thickness on the anodic oxidation time by using the FE-SEM images obtained after focused ion beam (FIB) milling (Fig. 4). The SnO_2 nanochannel array thicknesses were about 1.5, 2.3, 4.0, 6.0 and 7.0 μm for anodic oxidation times of 90, 150, 210, 270, 330 s, respectively. As shown in Fig. 5, the thickness increased linearly at the growth rate of about 1.47 μm min^{-1}. However, anodic oxidation longer than 330 s resulted in poor adhesion between the Sn metal substrate and the grown SnO_2 nanochannel arrays, leading to the partial peeling off. The thickness of the remaining SnO_2 nanochannel arrays on the Sn metal is shown in Fig. 4f. The thickness of SnO_2 nanochannel arrays was about 6.4 μm for an anodic oxidation time of 390 s, yielding thinner arrays than those for an anodic oxidation time of 330 s. As a result, the maximal thickness of SnO_2 nanochannel arrays was 7.0 μm, obtained for 330 s long anodic oxidation. It is noteworthy that the obtained vertically aligned pore structure was continuous without lateral cracks through this long range. Using the conventional anodic oxidation process, many lateral cracks were generated resulting in a discontinuous nanochannel structure,
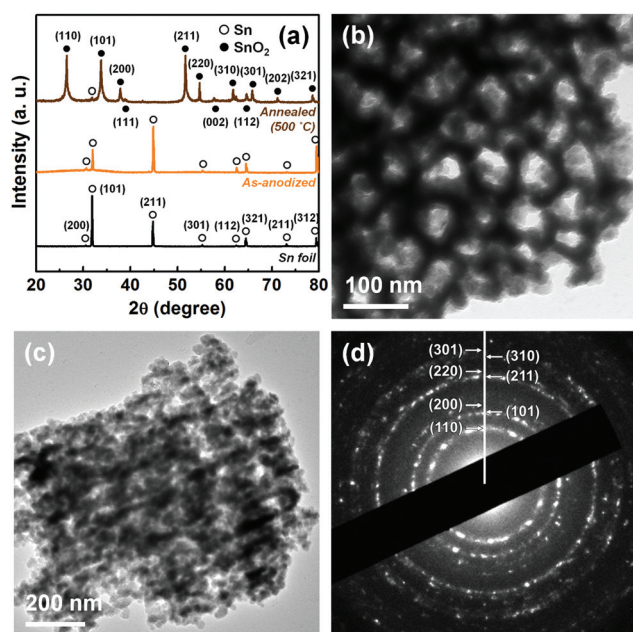

Fig. 3 (a) XRD patterns of Sn foil, as-anodized and annealed SnO_2 nanochannel arrays. TEM images (b, c) and SAED pattern (d) of annealed SnO_2 nanochannel arrays.
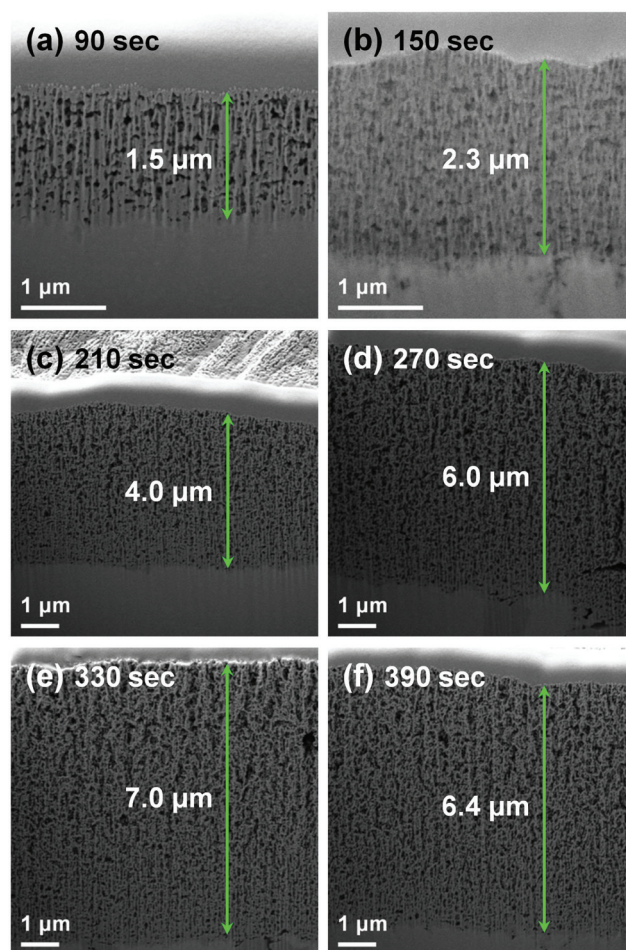

Fig. 4 Cross-sectional FE-SEM images (obtained after FIB-milling) of SnO_2 nanochannel arrays grown by anodic oxidation for 90–390 s.
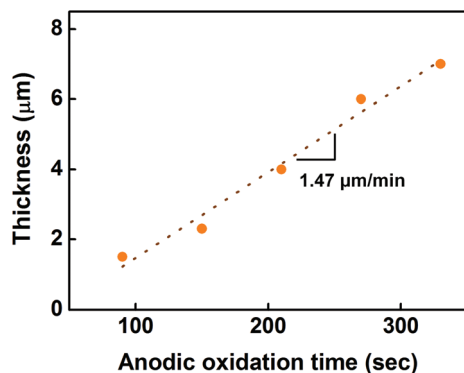
Fig. 5 Thicknesses of annealed SnO_2 nanochannel arrays prepared by ultrasonication, for different anodic oxidation times.

as shown in Fig. S1,† which is consistent with previous reports.[28–31] Crack creation was likely owing to the rapid anodic oxidation reaction and vigorous oxygen evolution, which created turbulence in the electrolyte and local stresses during the formation of SnO_2 nanochannels.[28] As already mentioned, ultrasonic waves assisted the oxygen gas to escape rapidly and smoothly, preventing the generation of lateral cracks as a consequence.

We utilized these SnO_2 nanochannel arrays with large-scale uniform structures as photoanodes in DSSCs. The SnO_2 nanochannel arrays were utilized directly, maintaining a vertically aligned structure as depicted in Fig. 6a. The whole size of the photoanode was 2.0 cm × 1.5 cm, and the active area was

0.25 cm². Polymer gel electrolytes containing iodide redox couples (I^-/I_3^-) and conventional Pt/FTO glass counter electrodes were utilized for the fabrication of the devices. The photocurrent density–voltage (J–V) characteristics for different anodic oxidation times are shown in Fig. 6b. For statistical significance, the J–V data were obtained from three cells for each electrode (Table S1†), and the average values are listed in Table 1 with the adsorbed amount of dye. The open-circuit voltage (V_{oc}) and fill factor (FF) did not significantly vary among the samples; however, the short-circuit photocurrent density (J_{sc}) strongly depended on the nanochannel thickness. This was attributed to the increased amount of the adsorbed dye molecules with increasing thickness. As a result, the conversion efficiency was optimized to be 1.29% at the largest thickness. According to the literature, conversion efficiencies of DSSCs with conventional SnO_2 nanoparticles were about 1.2–1.6% under one sun light intensity.[34,35,51] In this study, a polymer gel electrolyte was used instead of the conventional liquid-type electrolyte. A gel electrolyte is superior in stability; however, it is inferior to a liquid electrolyte considering the conversion efficiency of DSSCs. In addition, owing to the opaque Sn metal substrate, the J–V data were obtained under back-side illumination. Compared with the results for under front-side illumination, the conversion efficiency of the DSSC is generally decreased by about 40% under back-side illumination owing to the light absorption by the Pt/FTO glass counter electrode and electrolyte.[50] Considering these unfavorable conditions, the obtained conversion efficiency of 1.29% in this work is a promising result. This was attributed to the vertically aligned one-dimensional structure and to the uniform nanoporous surface structure of the SnO_2 nanochannel electrode, which are favorable for light absorption, electron collection and interfacial contact with the viscous gel electrolyte.[10,14]

Furthermore, it is noteworthy that the anodic oxidation time was significantly short (330 s) for achieving the optimal thickness for photovoltaic applications. Typically, for the preparation of TiO_2 or SnO_2 photoanodes in DSSCs, a viscous paste should be prepared via many complex steps including a sol–gel reaction, hydrothermal growth, and homogenization (mixing) processes. This process takes a long time, even up to several days. In this work, owing to the short anodic oxidation time and direct utilization of the anodized electrodes, the devices could be fabricated by a simple and rapid process. Even compared with the conventional anodic oxidation of Ti, the growth rate of the SnO_2 nanochannel in this study was much faster. The growth rate in the conventional anodic oxidation of Ti for achieving similar pore structures was reported to be about 50–300 nm min^{-1},[10–14,52,53] which is 5 to 30 times slower than that of the SnO_2 nanochannel in this study (1.47 µm min^{-1}). In addition, by employing a gel-type electrolyte instead of the conventional liquid electrolyte, the additional step of drilling and sealing small holes in the substrate for electrolyte injection could be omitted, allowing the whole process to be simpler and faster.

To further enhance the photovoltaic performance of the SnO_2 nanochannel electrode, a TiO_2 shell layer was deposited

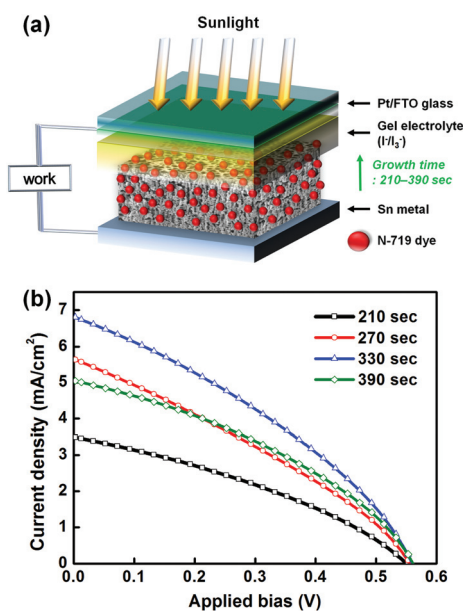**Fig. 6** (a) Schematic for the device structure of the dye-sensitized solar cell employing the SnO_2 nanochannel electrode. (b) Photocurrent density–voltage (J–V) characteristics of the SnO_2 nanochannel electrodes for different anodic oxidation times under standard 1 sun illumination (light intensity: 100 mW cm^{-2}, AM 1.5G filter).
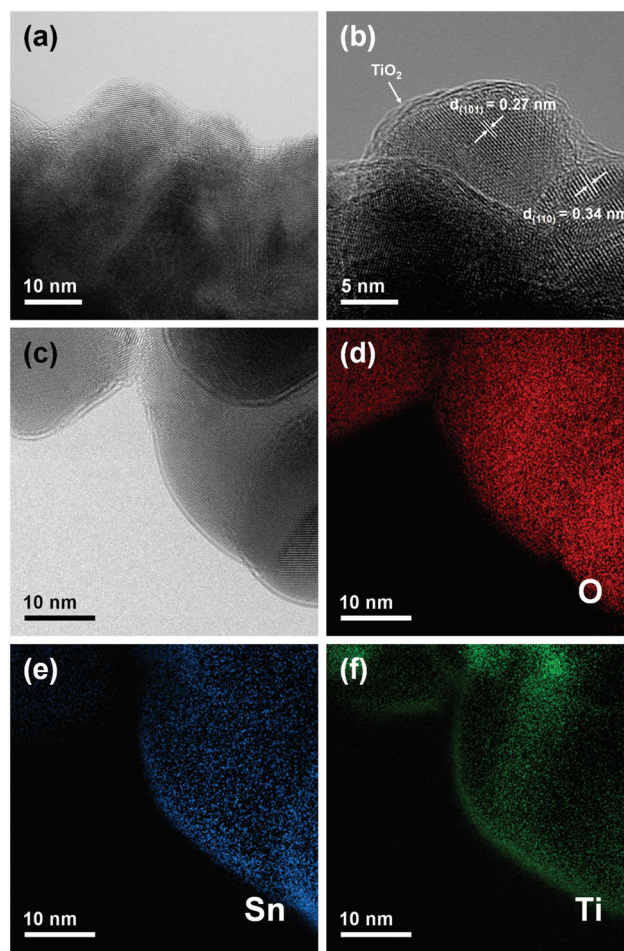
Table 1 Summary of the J–V characteristics of the SnO$_2$ nanochannel electrodes for different anodic oxidation times

Anodic oxidation time (s)/thickness (μm)	J_{sc} (mA cm^{-2})	V_{oc} (mV)	FF (%)	η (%)	Adsorbed amount of the dye (×10^{-8} mol cm^{-2})
210/4.0	3.50 ± 0.42	550 ± 15	34.20 ± 0.82	0.66 ± 0.05	6.51
270/6.0	5.45 ± 0.46	558 ± 17	32.99 ± 1.93	1.00 ± 0.05	9.18
330/7.0	6.72 ± 0.21	560 ± 10	34.19 ± 1.11	1.29 ± 0.04	9.51
390/6.4	5.56 ± 0.51	557 ± 7	33.80 ± 4.58	1.04 ± 0.06	9.23

onto the surface of nanochannel arrays. In particular, poor dye-loading and short electron lifetime of the SnO$_2$ electrode could be enhanced by using a TiO$_2$ shell layer.[34,35] For the TiO$_2$ deposition, we did not use solution-based methods such as the well-known TiCl$_4$ treatment;[34,54] rather, we used the ALD process to avoid further annealing. Additional annealing could increase the thickness of a compact SnO$_2$ barrier at the SnO$_2$ nanochannel/Sn metal interface, resulting in the increased internal resistance.[10,13] The TiO$_2$ shell layer thickness was controlled by varying the number of ALD cycles (3, 6, 15, 30 cycles). Fig. 7a–c show the TEM images of the SnO$_2$/TiO$_2$ nanochannel electrode prepared by using 15 ALD cycles. These images demonstrate that the prepared SnO$_2$ nanochannel is highly crystalline. In the high-resolution image (Fig. 7b), the (110) and (101) lattice planes (fringe spacing ∼0.34 and ∼0.27 nm, respectively) corresponding to the cassiterite SnO$_2$ phase are discernible.[55] In addition, the TiO$_2$ shell layer deposited onto the surface of the SnO$_2$ nanochannel is clearly seen. Furthermore, elemental energy-filtered (EF)-TEM maps (Fig. 7d–f) show that the TiO$_2$ shell layer is homogeneously distributed on the SnO$_2$ nanochannel surface. Fig. 8a–c show the X-ray photoelectron spectra (XPS) of the bare SnO$_2$ and SnO$_2$/TiO$_2$ nanochannel electrodes. The binding energies (BE) of Sn 3d$_{5/2}$ and O 1s were not noticeably different for both samples. The BEs of Sn 3d$_{5/2}$ and O 1s were 486.7 eV and 530.6 eV, respectively, which correspond to SnO$_2$.[56,57] In addition, the measured BEs of Ti 2p (458.9 eV and 464.8 eV for 2p$_{3/2}$ and 2p$_{1/2}$, respectively) indicate the presence of the TiO$_2$ shell.[58,59]

The dependence of J–V characteristics on the number of ALD cycles is shown in Fig. 9a. The J–V data were obtained from three cells for each electrode (Table S2†), and the average values are listed in Table 2 with the adsorbed amount of dye. As anticipated, the adsorbed amount of dye was increased by the deposition of the TiO$_2$ shell, owing to the higher isoelectric point for TiO$_2$, compared with SnO$_2$, in the dye solution.[35] However, the SnO$_2$/TiO$_2$ electrode prepared in 30 ALD cycles exhibited a lower adsorbed amount of dye compared with the bare sample. The reason for the reduction in the adsorbed amount of dye is that byproducts (i.e. HCl) of the reaction for TiO$_2$ ALD from TiCl$_4$ and H$_2$O were adsorbed on the interior surface of the porous nanochannel, occupying the adsorption sites for the dye-loading. In our previous study,[60] we found that HCl molecules, produced as a byproduct during the TiO$_2$ ALD process, could chemically adsorb on vacant sites prior to

Fig. 7 (a–c) TEM images of SnO$_2$/TiO$_2$ nanochannel arrays after 15 TiO$_2$ ALD cycles. (d–f) Elemental EF-TEM maps of O, Sn, and Ti for the image in (c).

the adsorption of TiCl$_4$. Furthermore, the occupancy of the adsorption sites by HCl molecules becomes much higher as the ALD cycle number increases. Therefore, it is believed that the reduction of the dye-loading in the 30 ALD-cycled electrodes can be attributed to the adsorption of byproducts, such as HCl, on the interior surface of the SnO$_2$/TiO$_2$ nanochannel, preventing the adsorption of the dye molecules.

As shown in Table 2, the V_{oc} and FF did not significantly depend on the presence of the TiO$_2$ shell layer. The trend of conversion efficiency was mainly affected by the J_{sc}. The elec-

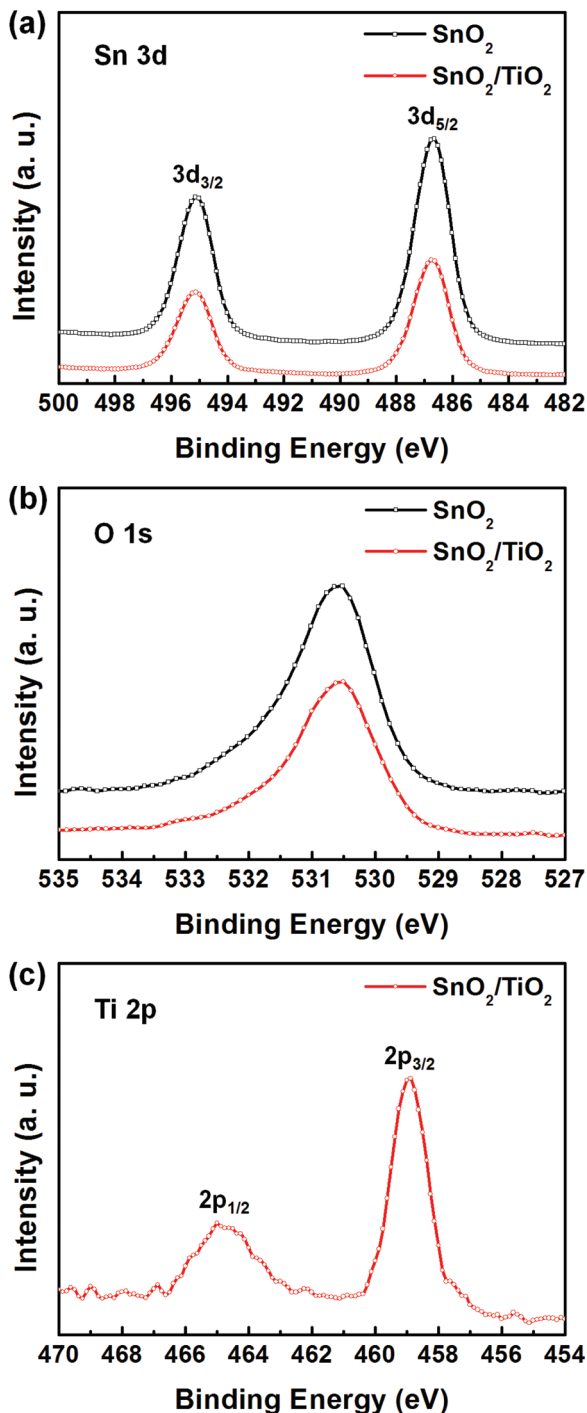**Fig. 8** XPS spectra of the bare SnO_2 and SnO_2/TiO_2 nanochannel electrodes prepared in 15 ALD cycles.

Fig. 9 (a) Photocurrent density−voltage (J−V) characteristics of the SnO_2/TiO_2 nanochannel electrodes vs. the number of TiO_2 ALD cycles, under standard 1 sun illumination (light intensity: 100 mW cm^{-2}, AM 1.5G filter). (b) Electrochemical impedance spectra of SnO_2 nanochannel electrodes under dark conditions with the bias potential of −0.5 V. The inset shows the equivalent circuit model.

trodes prepared in 3 and 6 cycles exhibited a lower J_{sc} and lower conversion efficiency than the bare electrode. However, the J_{sc} and conversion efficiency were enhanced and optimized in the electrode prepared in 15 cycles, where the J_{sc} and conversion efficiency increased by 20% and 19%, respectively, compared with the bare electrode. Because only a sub-monolayer can be grown by one ALD cycle, several cycles are required
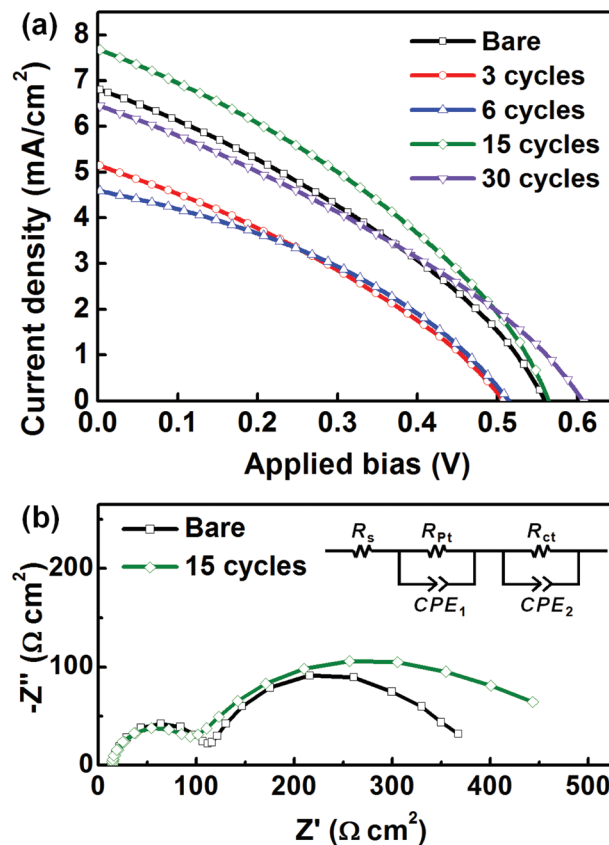
for forming a full monolayer by ALD. Considering the density (3.5–3.9 g cm^{-3}) of amorphous TiO_2 and the growth-per-cycle (~0.34 Å per cycle) in our ALD process,[61] about 8 to 10 cycles are required for forming a full monolayer of TiO_2. Therefore, 3 to 6 ALD cycles were not sufficient for forming a full monolayer of TiO_2. Such a sub-monolayer might unfavorably affect the photovoltaic performance, decreasing the electron injection and collection efficiency.[62] It is also believed that the thicker TiO_2 shell layer (15 cycles) can act as an energy barrier layer to prevent electron recombination between the SnO_2 electrode and the gel electrolyte,[35] consequently leading to the enhanced J_{sc} and conversion efficiency. The electrode with 30 cycles exhibited substantially enhanced V_{oc} compared with the bare electrode, implying that the coated layer efficiently reduced the electron recombination.[35,63] However, the J_{sc} decreased owing to the reduced adsorbed amount of dye, resulting in a similar conversion efficiency to that of the bare electrode.

To confirm the contribution of the TiO_2 shell layer to the electron recombination reduction, we performed the electrochemical impedance spectroscopy analysis. Fig. 9b shows Nyquist diagrams of DSSCs in the dark with the bias potential

Table 2 Summary of the J–V characteristics of the SnO_2/TiO_2 nanochannel electrodes for different numbers of TiO_2 atomic layer deposition cycles

ALD cycles	J_{sc} (mA cm^{-2})	V_{oc} (mV)	FF (%)	η (%)	Adsorbed amount of the dye ($\times 10^{-8}$ mol cm^{-2})
Bare	6.72 ± 0.21	560 ± 10	34.19 ± 1.11	1.29 ± 0.04	9.51
3 cycles	5.33 ± 0.51	495 ± 15	34.25 ± 1.51	0.90 ± 0.11	11.78
6 cycles	5.01 ± 0.65	500 ± 15	34.86 ± 2.79	0.87 ± 0.08	12.54
15 cycles	8.04 ± 0.51	560 ± 15	34.15 ± 1.32	1.53 ± 0.06	11.44
30 cycles	6.46 ± 0.03	595 ± 10	33.29 ± 0.92	1.28 ± 0.03	9.06

of −0.5 V. As shown in the inset, the equivalent circuit model comprises the series resistance (R_s), the impedance at the gel electrolyte/Pt counter electrode (R_{Pt} and CPE_1), and the impedance at the gel electrolyte/SnO_2 electrode (R_{ct} and CPE_2). The chemical capacitance (C_μ) of the SnO_2 electrode can be obtained from CPE_2. The impedance spectra were fitted by using the ZView software, and the obtained parameters are listed in Table 3. The interfacial charge transfer resistance (R_{ct}) was greatly increased by adding a TiO_2 shell layer, implying a significantly reduced electron recombination rate. The C_μ denotes the extent of electron accumulation in the photoanode, that is the SnO_2 electrode.[64] Under identical conditions (the same utilized electrolyte and the same bias potential), this value decreases as the conduction band potential of the photoanode exhibits a negative shift, because the bias potential denotes the energy difference between the redox potential of the electrolyte and the Fermi level of the photoanode.[65] Because the isoelectric point of TiO_2 is higher than that of SnO_2, resulting in the establishment of a surface dipole directed toward the SnO_2 core, the conduction band potential of the SnO_2 electrode can exhibit a negative shift by the TiO_2 shell deposition.[66] Therefore, the decreased C_μ for the SnO_2 nanochannel electrode with the TiO_2 shell indicates the negative shift of the conduction band potential. The electron lifetime, τ_n, can be evaluated from the product of R_{ct} and C_μ.[67] As shown in Table 3, the τ_n of the SnO_2 nanochannel electrode increased by 34% with the addition of the TiO_2 shell layer, implying that the TiO_2 shell layer contributed to more efficient electron collection in the photoanode.

It was reported that the conformal coating is not guaranteed only by using the typical ALD process, especially when the substrate has a nanoporous structure with high aspect ratio, such as nanotubular or nanochannel arrays.[68] The ALD process used in this work has not yet been optimized to be suitable for the SnO_2 nanochannel arrays. For the conformal coating of the shell layer onto the SnO_2 nanochannel arrays, the exposure times of precursors and purging times in the ALD process should be elaborately adjusted.[68,69] We expect that the conversion efficiency can be further enhanced by optimizing the ALD process for conformal coating of TiO_2 shells. In addition, in this work, the DSSCs were illuminated from the back-side for the J–V characterization, due to the opaque Sn metal substrate. For higher conversion efficiency, it is desirable to prepare the SnO_2 nanochannel arrays onto the transparent conducting glass substrate by depositing the Sn metal, followed by the anodic oxidation process.[13] These approaches are promising for realizing highly efficient DSSCs based on SnO_2 electrodes.

Conclusions

In summary, vertically aligned SnO_2 nanochannel arrays with large-scale uniform structures without lateral cracks were prepared by using a modified anodic oxidation process of the Sn metal. These vertically aligned arrays were directly and successfully applied in quasi-solid state DSSCs as photoanodes, yielding reasonable conversion efficiency under back-side illumination. Given that the anodic oxidation time was greatly short (330 s) for achieving the optimal thickness (7.0 μm) for the photovoltaic performance, the preparation process proposed in this study is a rapid and cost-effective one. In addition, the TiO_2 shell layer was coated by using the ALD process without further annealing. Owing to the enhanced dye-loading and increased electron lifetime with the TiO_2 shell, the J_{sc} and conversion efficiency were increased by 20% and 19%, respectively. These results provide important insight into the development of efficient electrode structures based on SnO_2 for photovoltaic applications by a simple, rapid, and low-cost fabrication process. Furthermore, we suggest that the large-scale vertically aligned SnO_2 nanochannel arrays developed in this study can also be effectively applied in other electrochemical devices such as sensors, capacitors, and lithium ion batteries.

Table 3 Parameters determined by fitting the impedance spectra of SnO_2 nanochannel electrodes obtained in the dark state at the bias potential of −0.5 V

ALD cycles	R_s (Ω cm^2)	R_{ct} (Ω cm^2)	C_μ (μF cm^{-2})	τ_n (ms)
Bare	14.20	254.8	699.2	178
15 cycles	13.73	390.9	612.6	239

Acknowledgements

Notes and references

1 Y. Xia, P. Yang, Y. Sun, Y. Wu, B. Mayers, B. Gates, Y. Yin, F. Kim and H. Yan, *Adv. Mater.*, 2003, **15**, 353.

2 M. M. Maqableh, X. Huang, S.-Y. Sung, K. S. M. Reddy, G. Norby, R. H. Victora and B. J. H. Stadler, *Nano Lett.*, 2012, **12**, 4102.

3 S. Wu, F. Wildhaber, O. Vazquez-Mena, A. Bertsch, J. Brugger and P. Renaud, *Nanoscale*, 2012, **4**, 5718.

4 J. Lin, K. Liu and X. Chen, *Small*, 2011, **7**, 1784.

5 Z. Zhang, L. Zhang, M. N. Hedhili, H. Zhang and P. Wang, *Nano Lett.*, 2013, **13**, 14.

6 S. D. Alvares, C. P. Li, C. E. Chiang, I. K. Schuller and M. J. Sailor, *ACS Nano*, 2009, **3**, 3301.

7 K.-S. Mun, S. D. Alvarez, W.-Y. Choi and M. J. Sailor, *ACS Nano*, 2010, **4**, 2070.

8 J. M. Macák, H. Tsuchiya, A. Ghicov and P. Schmuki, *Electrochem. Commun.*, 2005, **7**, 1133.

9 G. K. Mor, K. Shankar, M. Paulose, O. K. Varghese and C. A. Grimes, *Nano Lett.*, 2006, **6**, 215.

10 K. Zhu, N. R. Neale, A. Miedaner and A. J. Frank, *Nano Lett.*, 2007, **7**, 69.

11 K. Zhu, T. B. Vinzant, N. R. Neale and A. J. Frank, *Nano Lett.*, 2007, **7**, 3739.

12 G. K. Mor, S. Kim, M. Paulose, O. K. Varghese, K. Shankar, J. Basham and C. A. Grimes, *Nano Lett.*, 2009, **9**, 4250.

13 O. K. Varghese, M. Paulose and C. A. Grimes, *Nat. Nanotechnol.*, 2009, **4**, 592.

14 J.-Y. Kim, K. J. Lee, S. H. Kang, J. Shin and Y.-E. Sung, *J. Phys. Chem. C*, 2011, **115**, 19979.

15 A. Kongkanand, K. Tvrdy, K. Takechi, M. Kuno and P. V. Kamat, *J. Am. Chem. Soc.*, 2008, **130**, 4007.

16 W. Guo, X. Xue, S. Wang, C. Lin and Z. L. Wang, *Nano Lett.*, 2012, **12**, 2520.

17 L. Tao, Y. Xiong, H. Liu and W. Shen, *Nanoscale*, 2014, **6**, 931.

18 J. Z. Ou, R. A. Rani, M.-H. Ham, M. R. Field, Y. Zhang, H. Zheng, P. Reece, S. Zhuiykov, S. Sriram, M. Bhaskaran, R. B. Kaner and K. Kalantar-zadeh, *ACS Nano*, 2012, **6**, 4045.

19 J. Wu, L. Liu, S. Liu, P. Yu, Z. Zheng, M. Shara, Z. Zhou, H. Li, H. Ji and Z. M. Wang, *Nano Lett.*, 2014, **14**, 6002.

20 H. Qi, J. Wolfe, D. Wang, H. J. Fan, D. Fichou and Z. Chen, *Nanoscale*, 2014, **6**, 13457.

21 I. V. Sieber, H. Hildebrand, A. Friedrich and P. Schmuki, *Electrochem. Commun.*, 2005, **7**, 97.

22 H. Tsuchiya, J. M. Macak, L. Taveira and P. Schmuki, *Chem. Phys. Lett.*, 2005, **410**, 188.

23 S. Berger, F. Jakubka and P. Schmuki, *Electrochem. Commun.*, 2008, **10**, 1916.

24 N. R. de Tacconi, C. R. Chenthamarakshan, G. Yogeeswaran, A. Watcharenwong, R. S. de Zoysa, N. A. Basit and K. Rajeshwar, *J. Phys. Chem. B*, 2006, **110**, 25347.

25 Y.-C. Nah, A. Ghicov, D. Kim, S. Berger and P. Schmuki, *J. Am. Chem. Soc.*, 2008, **130**, 16154.

26 I. V. Sieber and P. Schmuki, *J. Electrochem. Soc.*, 2005, **152**, C639.

27 H. Tsuchiya and P. Schmuki, *Electrochem. Commun.*, 2005, **7**, 49.

28 H.-C. Shin, J. Dong and M. Liu, *Adv. Mater.*, 2004, **16**, 237.

29 L. Zaraska, N. Czopik, M. Bobruk, G. D. Sulka, J. Mech and M. Jaskula, *Electrochim. Acta*, 2013, **104**, 549.

30 J.-W. Lee, S.-J. Park, W.-S. Choi and H.-C. Shin, *Electrochim. Acta*, 2011, **56**, 5919.

31 A. Palacios-Padros, M. Altomare, A. Tighineanu, R. Kirchgeorg, N. K. Shrestha, I. Diez-Perez, F. Caballero-Briones, F. Sanz and P. Schmuki, *J. Mater. Chem. A*, 2014, **2**, 915.

32 A. N. M. Green, E. Palomares, S. A. Haque, J. M. Kroon and J. R. Durrant, *J. Phys. Chem. B*, 2005, **109**, 12525.

33 E. Ramasamy and J. Lee, *J. Phys. Chem. C*, 2010, **114**, 22032.

34 A. Kay and M. Grätzel, *Chem. Mater.*, 2002, **14**, 2930.

35 J.-Y. Kim, J. Y. Kim, D. K. Lee, B. Kim, H. Kim and M. J. Ko, *J. Phys. Chem. C*, 2012, **116**, 22759.

36 H. Tian, P.-H. Liu, F.-S. Meng, E. Gao and S. Cai, *Synth. Met.*, 2011, **121**, 1557.

37 N. K. Subbaiyan, E. Maligaspe and F. D'Souza, *ACS Appl. Mater. Interfaces*, 2011, **3**, 2368.

38 J. J. H. Pijpers, R. Koole, W. H. Evers, A. J. Houtepen, S. Boehme, C. D. M. Donega, D. Vanmaekelbergh and M. Bonn, *J. Phys. Chem. C*, 2010, **114**, 18866.

39 E. Ramasamy and J. Lee, *Energy Environ. Sci.*, 2011, **4**, 2529.

40 M. A. Hossain, G. Yang, M. Parameswaran, J. R. Jennings and Q. Wang, *J. Phys. Chem. B*, 2010, **114**, 21878.

41 J. J. Teh, G. H. Guai, X. Wang, K. C. Leong, C. M. Li and P. Chen, *J. Renewable Sustainable Energy*, 2013, **5**, 023120.

42 S. Ito, K. Nazeeruddin, P. Liska, P. Comte, R. Charvet, P. Péchy, M. Jirousek, A. Kay, S. M. Zakeeruddin and M. Grätzel, *Prog. Photovolt: Res. Appl.*, 2006, **14**, 589.

43 J. Park, H.-J. Koo, B. Yoo, K. Yoo, K. Kim, W. Choi and N.-G. Park, *Sol. Energy Mater. Sol. Cells*, 2007, **91**, 1749.

44 H. E. Prakasam, K. Shankar, M. Paulose, O. K. Varghese and C. A. Grimes, *J. Phys. Chem. C*, 2007, **111**, 7235.

45 S. K. Mohapatra, S. E. John, S. Banerjee and M. Misra, *Chem. Mater.*, 2009, **21**, 3048.

46 Pattern no. 41-1445, JCPDS 1996.

47 P. A. Russo, N. Donato, S. G. Leonardi, S. Baek, D. E. Conte, G. Neri and N. Pinna, *Angew. Chem., Int. Ed.*, 2012, **51**, 11053.

48 B. D. Cullity, *Elements of X-Ray Diffraction*, Addison-Wesley Pub. Co., Reading, Mass, 2nd edn, 1978.

49 A. Ghicov, S. P. Albu, R. Hahn, D. Kim, T. Stergiopoulos, J. Kunze, C.-A. Schiller, P. Falaras and P. Schmuki, *Chem. – Asian J.*, 2009, **4**, 520.

50 S. Ito, N.-L. C. Ha, G. Rothenberger, P. Liska, P. Comte, S. M. Zakeeruddin, P. Péchy, M. K. Nazeeruddin and M. Grätzel, *Chem. Commun.*, 2006, 4004.

51 C. Lee, G.-W. Lee, W. Kang, D.-K. Lee, M. J. Ko, K. Kim and N.-G. Park, *Bull. Korean Chem. Soc.*, 2010, **31**, 3093.

52 M. Paulose, K. Shankar, S. Yoriya, H. E. Prakasam, O. K. Varghese, G. K. Mor, T. A. Latempa, A. Fitzgerald and C. A. Grimes, *J. Phys. Chem. B*, 2006, **110**, 16179.

53 S. Sreekantan, K. A. Saharudin, Z. Lockman and T. W. Tzu, *Nanotechnology*, 2010, **21**, 365603.

54 P. M. Sommeling, B. C. O'Regan, R. R. Haswell, H. J. P. Smit, N. J. Bakker, J. J. T. Smits, J. M. Kroon and J. A. M. van Roosmalen, *J. Phys. Chem. B*, 2006, **110**, 19191.

55 C. Wang, Y. Zhou, M. Ge, X. Xu, Z. Zhang and J. Z. Jiang, *J. Am. Chem. Soc.*, 2010, **132**, 46.

56 S. Fujihara, T. Maeda, H. Ohgi, E. Hosono, H. Imai and S.-H. Kim, *Langmuir*, 2004, **20**, 6476.

57 L. Renard, J. Brotz, H. Fuess, A. Gurlo, R. Riedel and T. Toupance, *ACS Appl. Mater. Interfaces*, 2014, **6**, 17093.

58 T. Choudhury, S. O. Saied, J. L. Sullivan and A. M. Abbott, *J. Phys. D: Appl. Phys.*, 1989, **22**, 1185.

59 D. Gonbeau, C. Guimon, G. Pfister-Guillouzo, A. Levasseur, G. Meunier and R. Dormoy, *Surf. Sci.*, 1991, **254**, 81.

60 I. Park, J. Leem, H.-Y. Lee and Y.-S. Min, *Bull. Korean Chem. Soc.*, 2013, **34**, 519.

61 G. Triani, P. J. Evans, D. R. G. Mitchell, A. J. Attard, K. S. Finnie, M. James, T. Hanley, B. Latella, K. E. Prince and J. Bartlett, Advances in Thin-Film Coatings for Optical Applications II (Proceedings of SPIE), SPIE, Bellingham, WA, 2005, vol. 5870, p. 587009.

62 M. Law, L. E. Greene, A. Radenovic, T. Kuykendall, J. Liphardt and P. Yang, *J. Phys. Chem. B*, 2006, **110**, 22652.

63 Y. Diamant, S. Chappel, S. G. Chen, O. Melamed and A. Zaban, *Coord. Chem. Rev.*, 2004, **248**, 1271.

64 F. Fabregat-Santiago, J. Bisquert, E. Palomares, L. Otero, D. Kuang, S. M. Zakeeruddin and M. Grätzel, *J. Phys. Chem. C*, 2007, **111**, 6550.

65 S. E. Koops, B. C. O'Regan, P. R. F. Barnes and J. R. Durrant, *J. Am. Chem. Soc.*, 2009, **131**, 4808.

66 Q. Zhang and G. Cao, *Nano Today*, 2011, **6**, 91.

67 F. Fabregat-Santiago, G. Garcia-Belmonte, I. Mora-Seró and J. Bisquert, *Phys. Chem. Chem. Phys.*, 2011, **13**, 9083.

68 H.-Y. Lee, C. J. An, S. J. Piao, D. Y. Ahn, M.-T. Kim and Y. S. Min, *J. Phys. Chem. C*, 2010, **114**, 18601.

69 C. Marichy, M. Bechelany and N. Pinna, *Adv. Mater.*, 2012, **24**, 1017.

Electronic supplementary information

Highly uniform and vertically aligned SnO$_2$ nanochannel arrays for photovoltaic applications

Jae-Yup Kim,‡[a] Jin Soo Kang,‡[bc] Junyoung Shin,[c] Jin Kim,[bc] Seung-Joo Han,[d] Jongwoo Park,[a] Yo-Sep Min,[d] Min Jae Ko*[aef] and Yung-Eun Sung*[bc]

[a]Photo-electronic Hybrids Research Center, Korea Institute of Science and Technology (KIST), Seoul 136-791, Republic of Korea.

[b]Center for Nanoparticle Research, Institute for Basic Science (IBS), Seoul 151-742, Republic of Korea.

[c]School of Chemical and Biological Engineering, Seoul National University, Seoul 151-742, Republic of Korea.

[d]Department of Chemical Engineering, Konkuk University, Seoul, 143-701, Republic of Korea

[e]Green School, Korea University, Seoul 136-701, Republic of Korea.

[f]KU-KIST Graduate School of Converging Science and Technology, Korea University, Seoul 136-701, Republic of Korea.

‡These authors contributed equally to this work.
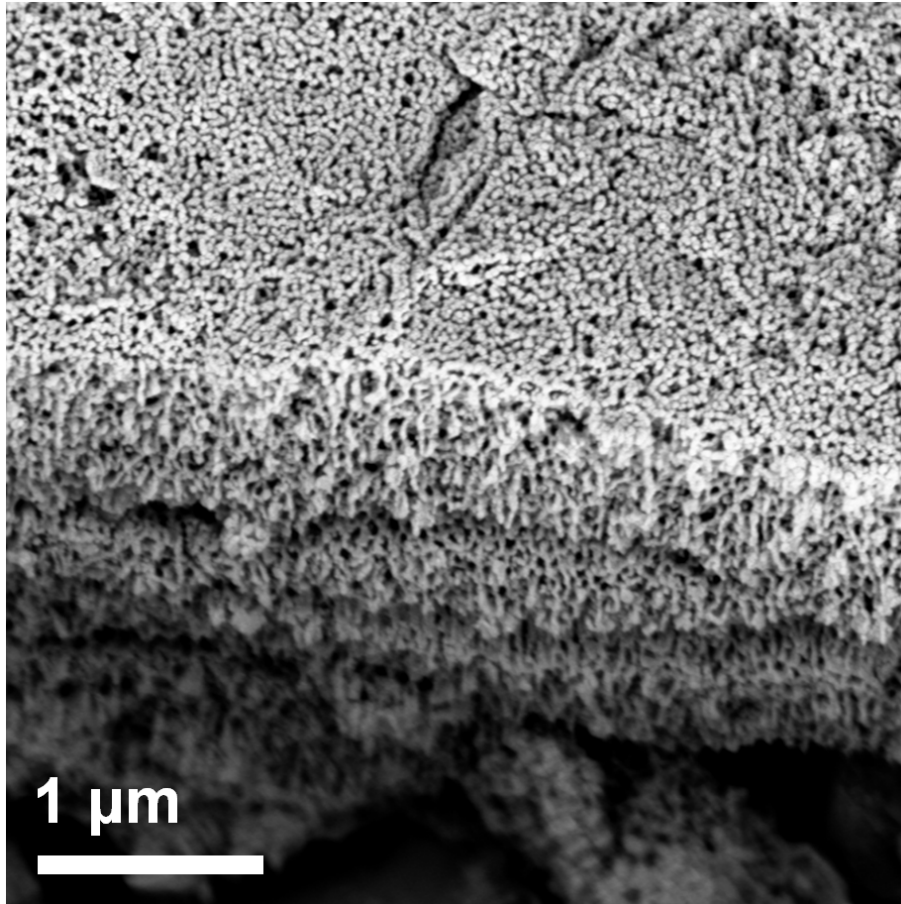
*CORRESPONDING AUTHORS

Yung-Eun Sung

Tel: +82-2-880-1889; fax: +82-2-888-1604; e-mail address: ysung@snu.ac.kr

Min Jae Ko

Tel: +82-2-958-5518; fax: +82-2-958-6649; e-mail address: mjko@kist.re.kr

Fig. S1. FE-SEM image of annealed SnO_2 nanochannel arrays prepared by the conventional anodic oxidation process (This image was obtained after tilting the edge side of prepared sample during the FE-SEM analysis).

Table S1. Summary of *J-V* characteristics of the SnO$_2$ nanochannel electrodes for different anodic oxidation times.

anodic oxidation time (sec)	thickness of nanochannel (μm)	J_{sc} (mA/cm^2)	V_{oc} (mV)	FF (%)	η (%)
210	4.0	3.92	535	33.38	0.70
		3.49	550	34.38	0.66
		3.10	565	34.83	0.61
270	6.0	5.73	545	31.06	0.97
		5.64	555	31.31	0.98
		4.99	575	36.59	1.05
330	7.0	6.81	560	34.09	1.30
		6.85	550	33.18	1.25
		6.51	570	35.30	1.31
390	6.4	5.65	550	35.40	1.10
		5.99	560	29.22	0.98
		5.05	560	36.78	1.04

Table S2. Summary of the *J-V* characteristics of the SnO_2/TiO_2 nanochannel electrodes for different number of TiO_2 atomic layer deposition cycles.

ALD cycles	J_{sc} (mA/cm^2)	V_{oc} (mV)	*FF* (%)	η (%)
0 cycle-1	6.81	560	34.09	1.30
0 cycle-2	6.85	550	33.18	1.25
0 cycle-3	6.51	570	35.30	1.31
3 cycles-1	5.15	510	32.74	0.86
3 cycles-2	5.84	485	35.31	1.00
3 cycles-3	5.00	490	34.69	0.85
6 cycles-1	4.59	515	37.65	0.89
6 cycles-2	4.78	490	33.73	0.79
6 cycles-3	5.66	495	33.19	0.93
15 cycles-1	8.55	570	32.83	1.60
15 cycles-2	7.90	545	34.37	1.48
15 cycles-3	7.68	565	35.26	1.53
30 cycles-1	6.45	605	32.80	1.28
30 cycles-2	6.45	590	32.85	1.25
30 cycles-3	6.49	590	34.21	1.31